Materials Advances

PAPER

View Article Online
View Journal | View Issue

Cite this: *Mater. Adv.*, 2024, 5, 8097

Construction of a 3D flower-like NiO/Mn_3O_4 heterojunction using Tulsi leaf extract for enhanced photodegradation of thiamethoxam pesticide and organic dyes under direct sunlight†

Mandvi,[a] Prit Pal Singh,[a] Suhas Ballal,[b] Mamta Chahar,[c] Jaya Bansal,[d] Ranvijay Kumar,[e] Sandeep Kumar[f] and Sandeep Kaushal *[g]

The construction of high-efficiency photocatalysts for photocatalytic disintegration of organic contaminants is a significant challenge. Herein, novel porous flower-like NiO/Mn_3O_4 heterojunction photocatalysts were successfully designed *via* a green synthesis route employing Tulsi leaf extract. The NiO/Mn_3O_4 heterojunction photocatalyst exhibited exceptional activity in the decomposition of thiamethoxam pesticide and crystal violet and rhodamine B dyes. The studied X-ray diffraction pattern established the existence of both NiO and Mn_3O_4 in the heterojunction photocatalyst. Field emission scanning electron microscopy micrographs substantiated the porous flower-like structure of the photocatalyst. Surface study demonstrated the surface area, micropore volume and mean pore diameter of the photocatalyst to be 119.93 $m^2\ g^{-1}$, 0.1859 $cm^3\ g^{-1}$ and 3.78 nm, respectively, which are highly favourable for surface interactions. Photocatalytic experiments revealed that the heterojunction (NM-I) showed the highest photocatalytic efficiency for the degradation of thiamethoxam pesticide (93% in 90 min) and crystal violet (93.6% in 80 min) and rhodamine B (93.2% in 80 min) dyes with a rate constant of 0.0212, 0.0378 and 0.0355 min^{-1}, respectively. The performance of the NiO/Mn_3O_4 heterojunction was optimized by investigating the roles of certain variables, including pH, catalyst dosage, and scavengers, in degrading organic pollutants. Moreover, liquid chromatography–mass spectrometry was utilized to predict a tenable mechanism for thiamethoxam disintegration. In addition, the catalyst showed excellent stability and reusability, and was simple to extract from the solution. After five cycles, thiamethoxam, crystal violet and rhodamine B elimination efficiencies were 82%, 84%, and 87%, respectively.

Received 12th July 2024,
Accepted 10th September 2024

DOI: 10.1039/d4ma00708e

rsc.li/materials-advances

Open Access Article. Published on 10 September 2024. Downloaded on 2/24/2026 11:31:03 PM.
This article is licensed under a Creative Commons Attribution 3.0 Unported Licence.

1. Introduction

It is widely accepted that many environmental contaminants are inevitable consequences of human activities, including industrialization and agricultural practices.[1] On account of their extensive use in agriculture and inappropriate wastewater disposal practices, pesticides used to safeguard plants from weeds, fungi, and insects are the noteworthy contaminants of natural water (surface water and groundwater).[2] According to UN reports, a mere 1% of pesticides utilized in agriculture truly reach the crops, and only 5% of the pesticides target the pests. As a result, pesticide residues contaminate practically every aspect of our ecosystem, such as the land, air, and, especially, water.[3,4] Pesticide pollution can have a serious impact on the ecosystem, including on fish, birds, plants, insects, and soil microbes as well as on the well-being of humans. Therefore, roughly 2 million toxic human exposures and 10 000 deaths caused by pesticides worldwide each year are not shocking.[5] However, without pesticides, yields might drop by up to one-third, which would result in a 75% increase in food prices.[6] For this reason, pesticide usage is unavoidable in the best interests of agribusiness.

Thiamethoxam (TMX), a pesticide composed of the naturally occurring toxin neonicotinoid, is a perfect example of a material that is frequently found in fresh water. When it first came into effect for crop protection, it was believed to be an

---

[a] *Sri Guru Granth Sahib World University, Fatehgarh Sahib, Punjab, India*
[b] *Jain (Deemed-to-be University), Banglore, Karnataka, India*
[c] *NIMS Institute of Engineering and Technology, NIMS University, Jaipur, Rajasthan, India*
[d] *Chandigarh Engineering College, Jhanjeri, Mohali, Punjab, India*
[e] *University Centre for Research and Development, Chandigarh University, Gharuan, Mohali, Punjab, India*
[f] *Akal University, Talbwandi Sabo, Punjab, India*
[g] *Regional Institute of Education, NCERT, Ajmer, Rajasthan, India. E-mail: kaushalsandeep33@gmail.com*

† Electronic supplementary information (ESI) available. See DOI: **https://doi.org/10.1039/d4ma00708e**

© 2024 The Author(s). Published by the Royal Society of Chemistry

Open Access Article. Published on 10 September 2024. Downloaded on 2/24/2026 11:31:03 PM.
This article is licensed under a Creative Commons Attribution 3.0 Unported Licence.

ecologically sound compound. This pesticide protects a variety of crops, including premium fruits, vegetables, and cereals, by disrupting the neurological system of pests, such as whiteflies, aphids, and micro-lepidoptera.[7,8] As TMX is a persistent and exceptionally soluble chemical (4.1 g L^{-1}), it can accumulate over time in soil and aquatic ecosystems.[9,10] The recent use of TMX in several nations has suggested a direct detrimental effect on the ecosystem and the food chain.[11] A study of TMX's toxicity showed that bacteria and algae could be harmed by the chemical and its intermediates created during the disinfestation operation.[12] Currently, TMX is illegitimate in the European Union, while the Environmental Protection Agency (EPA) of the USA normally reappraises the environmental hazard assessment and guidelines for harvests in successive publishable regulations entitled "Thiamethoxam; Pesticide Tolerance".

With the increase in worldwide textile dye production, increasing water sources are being polluted as toxic substances find their way into rivers, ponds, and lakes through various channels, jeopardizing the healthy development of the ecosystem.[13] Approximately 15% of synthetic waste from industry, especially related to textiles and pharmaceuticals, is reportedly inadvertently paired with the primary freshwater flow.[14] Environmental protection remains the primary concern because the tainted matrix in the drinking water stream progressively hinders exposure to sunlight, affecting the aquatic environment's microbial activities.[15] Decolourization poses a significant difficulty because the dye molecules in waste water are inert to light, heat, and oxidant radicals.[16]

Because pesticides and dyes are the major cause of water contamination, eco-friendly or simple solutions are needed to clean the contaminated water and restore it to an environment that is suitable for humans and other living beings. The treatment for water contaminated with pesticides and dyes includes chemical, physical, and biological processes which have shown promising results in the past. Several techniques, including biological treatments, oxidation, electrolysis, adsorption, liquid membrane separation, and chemical catalytic degradation, in addition to a few widely utilized techniques, such as ultrafiltration, desalination, and reverse osmosis[17,18] are utilized for the elimination of pollutants from waste water. There are differences in the cost, environmental effects, and degradation effectiveness of different chemical and physical approaches. Although these processes can sporadically remove harmful pollutants, they can also produce unintended compounds and raise health risks.[19] Among all the above approaches, photocatalysis is the most relevant and effective in converting potentially dangerous substances into non-toxic ones. For photocatalysis, the fabrication of a competent and economical photocatalyst is crucial that might be proficient in degrading organic pollutants, such as TMX and crystal violet (CV). The common metal oxide semiconductors which are more appropriate for photocatalysis, are TiO_2, CdS, ZnS, ZnO, NiO, CuO and Mn_3O_4.[20,21]

Mn_3O_4 is predominantly noteworthy because it is a heterogeneous valent transition metal oxide. It is a semiconductor with a wide band gap that exhibits remarkable thermodynamic properties, comparatively high conductivity, chemical stability, and a range of fascinating chemical and physical characteristics. Furthermore, because of its exceptional qualities, Mn_3O_4 is a potential transitional p-type metal oxide.[22] Similarly, NiO NPs have attracted interest due to their large surface area, good chemical resistance, superior electronic conductivity, and super conductance features.[23] The sustainable nature with extraordinary reactivity of the NiO NPs makes them possible contenders in various applications.[24,25]

Metal oxides and their composites are currently fabricated using various chemical methods, including hydrothermal, sol gel, ball milling, co-precipitation, electro-spinning, wet deposition, and surface coating. Currently, the fabrication of compounds employing biological substances is a hot topic for researchers. Various extracts have been used in a few green technology initiatives to produce NPs.[26–29]

Metal oxide photocatalysts are widely utilized in photocatalysis and have excellent illumination capabilities, but their everyday use is hampered by a few related problems.[30] The fast recombination rate of photo-generated electron–hole pairs is problematic for them to serve as a photocatalyst. Because metal oxides often have broad band gaps, higher energy radiation is required for the creation of electron–hole pairs. Consequently, they behave as inactive catalysts in visible light that constitutes a sizable proportion of the solar spectrum.[31] Furthermore, the materials may protect the catalyst surface in certain photocatalytic reactions, prohibiting charges from interacting with the intended molecules and deactivating the catalyst. To alleviate the disadvantages related to pristine metal oxide nanoparticles, numerous approaches, including the construction of heterojunctions with other semiconductors to enhance charge separation and transfer; doping with other metals and metal oxides to maintain charges distantly; and augmenting optical absorption, metal deposition, and surface alteration with inorganic acids, have been used.[32]

Enthused by the aforementioned divulgence, a novel NiO/Mn_3O_4 heterojunction photocatalyst was synthesized in an eco-friendly way using *Ocimum tenuiflorum* (Tulsi leaves). The Tulsi leaf extract was used as a solvent for the biogenic synthesis of NiO/Mn_3O_4 heterojunction. The properties of the fabricated NiO/Mn_3O_4 heterojunction were analysed by employing various sophisticated techniques. Eventually, the biogenic synthesized NiO/Mn_3O_4 heterojunction was utilized for the efficient photodegradation of the TMX pesticide and model dye CV and rhodamine B (RhB) in effluents under sunlight irradiation. Consequently, this study contributes to the body of knowledge already available on the creation of affordable and environment friendly photocatalysts that have a high degrading performance with no impact on the environment while eradicating harmful compounds from contaminated water.

2. Experimental

2.1 Materials and reagents

The chemicals used to synthesize NiO and Mn_3O_4 metal oxide nanoparticles include nickel nitrate (LOBA Chemie Pvt. Ltd),

© 2024 The Author(s). Published by the Royal Society of Chemistry

Open Access Article. Published on 10 September 2024. Downloaded on 2/24/2026 11:31:03 PM.
This article is licensed under a Creative Commons Attribution 3.0 Unported Licence.

manganese acetate (LOBA Chemie Pvt. Ltd), fresh green Tulsi leaves, ethanol (Changshu Hongsheng Fine Chemical Co. Ltd) and double distilled water. The chemicals employed in this investigation were of analytical grade.

2.2 Tulsi leaf extract preparation

The leaf extract was synthesized by washing fresh Tulsi leaves (10 g) repeatedly with double distilled water. The washed leaves were grounded, transferred to a 250 mL beaker and boiled for 1 h after adding 100 mL of double distilled (DD) water. The leaf extract was filtered using Whatman filter paper after cooling to an ambient temperature. The centrifugation of the filtrate at 7000 rpm was carried out for about 30 min. The collected supernatant was kept at 4 °C and was used as a capping, reducing, and stabilizing agent.

2.3 Synthesis of Mn_3O_4 Nanoparticles

After the addition of 3.67 g of manganese acetate to 50 mL of distilled water, the solution was sonicated for 30 min. Then, 20 mL of Tulsi leaf extract was added to this solution and heated to 80 to 90 °C for 5 h at pH 7 with constant stirring. The reaction mixture was centrifuged at 4000 rpm for 20 min. After three rounds of washing with DD water and ethanol, the resulting NPs were dried in an air oven at 150 °C and then calcined for 3 h at 80 °C in an air furnace. The resulting green Mn_3O_4 NPs were labelled as Tulsi-Mn_3O_4 and stored in a glass bottle.

2.4 Synthesis of NiO nanoparticles

$NiNO_3·6H_2O$ (4.3 g) was added to 50 mL of DD water in a round-bottom flask and sonicated for 30 min, followed by the addition of 20 mL of Tulsi leaf extract. The ensuing mixture was heated at 90 °C for 5 h with constant stirring at pH 7. After centrifugation of the mixture at 4000 rpm for 25 min, the resultant Tulsi-NiO nanoparticles were cleaned three times using DD water and ethanol. The obtained NPs were dried for a day at 150 °C in an incubator, followed by calcination for 3 h at 80 °C in an air furnace. The NPs were examined using various spectroscopic and microscopic methods.

2.5 Synthesis of NiO/Mn_3O_4 heterojunction

To prepare NiO/Mn_3O_4 heterojunction, $NiNO_3·6H_2O$ (0.3 M) and $Mn(CH_3COO)_2$ (0.3 M) were added to 50 mL of DD water in a 250 mL round bottom flask and stirred for 30 min. Then, 30 mL of green extract (Tulsi) was added very slowly to the reaction mixture and stirred at 90 °C for two days. The obtained mixture was kept for 16 h and then centrifuged at 4500 rpm for 30 min. The washing of the obtained nanoparticles was carried out three times using distilled water and ethanol. The nanocomposite was dried in an air oven at 80 °C for one day, followed by calcination in an air furnace at 450 °C for 4 h. Three different NiO/Mn_3O_4 heterojunction photocatalysts were synthesized using the same process by changing the mole ratio of NiO : Mn_3O_4 to 1 : 1 (NM-I), 0.5 : 1 (NM-II), and 1 : 0.5 (NM-III).

2.6 Photocatalytic activity

The photodecomposition of TMX pesticide, CV and RhB dyes was performed to assess the catalytic behaviour of the obtained heterojunction in sunlight. A UV-vis spectrophotometer was used to record the absorption spectra of TMX, CV and RhB solutions to chart the time-dependent change in the concentration of solution. In this context, NiO/Mn_3O_4 heterojunction (10–50 mg) was introduced in 50 mL solutions (20 mg L^{-1}) of various pollutants taken in separate beakers. Prior to exposure to sunlight, the suspensions were shaken for 30 min in the dark to acquire adsorption–desorption equilibrium. Aliquots were taken from the suspension at predetermined intervals when exposed to light, centrifuged at 3500–4500 rpm for 10 min, and then filtered. Using absorbance measurements at the absorption maxima of the contaminants (250 nm for TMX, 585 nm for CV, and 554 nm for RhB), the concentration of pollutants was determined. LCMS was used to identify TMX photodegradation intermediates, as explained in the supplementary information. The % deterioration of pollutants with heterojunction catalysts was assessed as follows:

$$\%\mathrm{Degradation} = \frac{C_e - C_t}{C_e} \times 100,$$

where C_e is the concentration at equilibrium and C_t at time t. The kinetics of the decomposition reaction of TMX, CV and RhB were examined using the first-order kinetic equation based on the Langmuir–Hinshelwood kinetic model.

The NiO/Mn_3O_4 heterojunction catalyst's durability and reusability were also assessed by reusing the catalyst's particles while performing the same tests repeatedly throughout five cycles. For each cycle, catalysts were recycled after performing centrifugation and washing in ethanol and DD water.

A radical trapping investigation was performed to recognise the main reactive intermediates involved in the photocatalytic decomposition pathway. A specific amount of radical scavengers, including *p*-benzoquinone (BQ), potassium dichromate ($K_2Cr_2O_7$), isopropyl alcohol (IPA) and triethylamine (TEA), were introduced in the reaction mixture to identify various reactive oxygen intermediates involved in the decomposition of pollutants.

3. Results and discussion

3.1 Characterization of NiO/Mn_3O_4 heterojunctions

3.1.1 Diffused reflectance spectroscopy evaluation. UV-vis diffuse reflectance spectroscopy (DRS) of NiO, Mn_3O_4 and NiO/Mn_3O_4 heterojunctions was performed (Fig. S1, ESI†). The band gap (E_g) energies of NiO and Mn_3O_4 were estimated to be 2.78 eV and 2.24 eV, respectively, which correspond to those documented in the literature.[33,34] The band gaps of NiO/Mn_3O_4 heterojunction samples, *i.e.* NM-I, NM-II and NM-III, were observed to be 2.39, 2.67, and 2.54 eV, respectively, indicating that the band gap of NiO has diminished due to incorporation of Mn_3O_4. Furthermore, some extra bonds emerge when two distinct semiconductors are combined to construct a

Open Access Article. Published on 10 September 2024. Downloaded on 2/24/2026 11:31:03 PM.
This article is licensed under a Creative Commons Attribution 3.0 Unported Licence.

heterojunction owing to the increase in the total number of molecular orbitals. The difference between the bonding and antibonding molecular orbitals becomes smaller with an increase in the number of molecular orbitals. Therefore, a heterojunction has a narrower band gap than a pure semiconductor. Moreover, this decrease in the band gap supports electronic coupling among Mn_3O_4 and NiO.

3.1.2 FT-IR investigation. The FTIR spectra of the synthesized materials with diverse mole proportions are presented in Fig. S2 (ESI†). The peak at 1643 cm^{-1} is ascribed to the C$=$O of ester groups. The C$=$C absorption band typical of lignin is noticed at 1523 cm^{-1}. The band at 1320 cm^{-1} specifies S$=$O stretching of the sulphated polysaccharide unit. The ethers and glyosidic of carbohydrates may be the cause of the C–O vibrational peaks observed at 1033 cm^{-1}. The characteristic peak at 646 cm^{-1} indicated Ni–O stretching.[35] The IR spectrum of green synthesized Mn_3O_4 NPs shows an absorption band centered at 645 cm^{-1}, indicating coupling among the Mn–O stretching modes in the distorted vibration of Mn–O in an octahedral environment. The appearance of the aforesaid absorption band offers conclusive proof of the formation of Mn_3O_4.[36] The peaks located at 3744 and 1670 cm^{-1} are attributed to the vibrations of the O–H bond of the adsorbed water molecules. The IR bands observed in the synthesized Mn_3O_4 NPs conform with those of the reported Mn_3O_4 materials.[37] The coexistence of NiO and Mn_3O_4 semiconductors in the composite was confirmed by the infrared data of composites with various ratios.

3.1.3 X-ray diffraction studies. The X-ray diffraction patterns of the NiO, Mn_3O_4, and NiO/Mn_3O_4 heterojunction catalysts are illustrated in Fig. 1. The lattice planes (111), (200), (220), (311), and (222) are represented by the peaks (*hkl*) in the XRD patterns of NiO NPs, which are located at 2θ = 37.3, 43.3, 62.9, 75.6, and 79.6°, respectively. The diffraction pattern of the synthesized NPs revealed a fcc structure with a mean lattice parameter of 4.17710 Å, which is consistent with JCPDS card number 47-1049.[25] The fact that the products have crystallized and that there are no noticeable peaks due to impurity phases, suggesting that the green method of producing NiO crystals was successful. The XRD pattern of Mn_3O_4 NPs, however, exhibits peaks (*hkl*) at 2θ = 18.0, 28.9, 32.4, 36.1 and 60.1° corresponding to the lattice planes (101), (112), (103), (211) and 224, respectively. The XRD pattern of as-synthesized Mn_3O_4 NPs displays ample sharp peaks matching JCPDS no. 96-151-4122, signifying the creation of a tetragonal Hausmannite-type structure (space group: *I*41/*am*).[30] NiO and Mn_3O_4 coexisted as distinct phases in the NiO/Mn_3O_4 heterojunction, as evidenced by the appearance of diffraction peaks of both the NiO and Mn_3O_4 NPs.

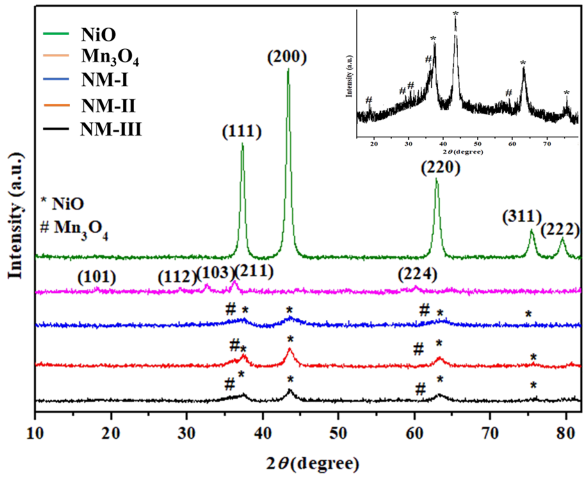

Fig. 1 XRD patterns of pure NiO, Mn_3O_4 and NiO/Mn_3O_4 heterojunction samples.

3.1.4 FESEM analysis. The morphology of the as-synthesized NiO/Mn_3O_4 heterojunction sample was explored by the FESEM, as depicted in Fig. 2. The obtained NiO/Mn_3O_4 heterojunction is composed of a flower-like structure (Fig. 2(a)). The NiO/Mn_3O_4 heterojunction flowers with distorted spherical symmetry can be observed in detail from the side (Fig. 2(b)), which clearly illustrates that they are formed by numerous interconnected large nanosheets. However, the FESEM micrograph of pristine NiO and Mn_3O_4 nanoparticles exhibited a sheet-like and agglomerated rod-like structures, respectively (Fig. S3, ESI†). An energy dispersive spectroscopy (EDS) study was performed to evaluate the elements present in NiO/Mn_3O_4 heterojunction. The skeleton function of the fabricated heterojunction may homogeneously scatter the constituent elements and prevent their agglomeration, as shown in Fig. 2(c), which also displays elemental mapping pictures of homogeneously scattered Ni, Mn, and O elements.

3.1.5 High resolution transmission electron microscopy (HRTEM). The morphology of NiO NPs, Mn_3O_4 NPs and NiO/Mn_3O_4 heterojunction prepared by green route was studied by HRTEM. The biogenic synthesized pure NiO and Mn_3O_4 NPs have agglomerated quasi spherical and distorted rod-like structures, respectively (Fig. S4, ESI†). HRTEM pictures of the biogenic synthesized heterojunction at different scale bars are shown in Fig. 3(a)–(c). The regular cubic structures of the heterojunction are shown in Fig. 3(b). To observe the lattice fringes of the as-synthesized heterojunction, a specific area was chosen (Fig. 3(d) and (e)). According to Fig. 3(d), the lattice fringes are analogous to Mn_3O_4 NPs with an interplanar spacing of 0.27 nm which is related to the (103) lattice plane. Similarly, the (200) plane of lattice orientation is relevant for the NiO structure (Fig. 3(e)) with interplanar spacing of 0.21 nm. The crystalline nature of the NiO/Mn_3O_4 heterojunction is established by the SAED pattern (Fig. 3(f)). The SAED pattern endorses that the NiO/Mn_3O_4 heterojunctions are polycrystalline in nature and indexed to (211), (111) and (200) planes, which are in good agreement with the XRD results.

3.1.6 Surface area measurement. The Brunauer–Emmett–Teller (BET) technique was used to examine the textural properties of the as-synthesized NiO/Mn_3O_4 heterojunction (Fig. S5, ESI†). The type-IV isotherm and H3 hysteresis loop indicate that the prepared catalyst has a mesoporous structure. According to the BET, the specific surface area, mean pore diameter and micropore volume were found to be 119.93 $m^2\ g^{-1}$, 3.78 nm and

© 2024 The Author(s). Published by the Royal Society of Chemistry

Open Access Article. Published on 10 September 2024. Downloaded on 2/24/2026 11:31:03 PM.
This article is licensed under a Creative Commons Attribution 3.0 Unported Licence.

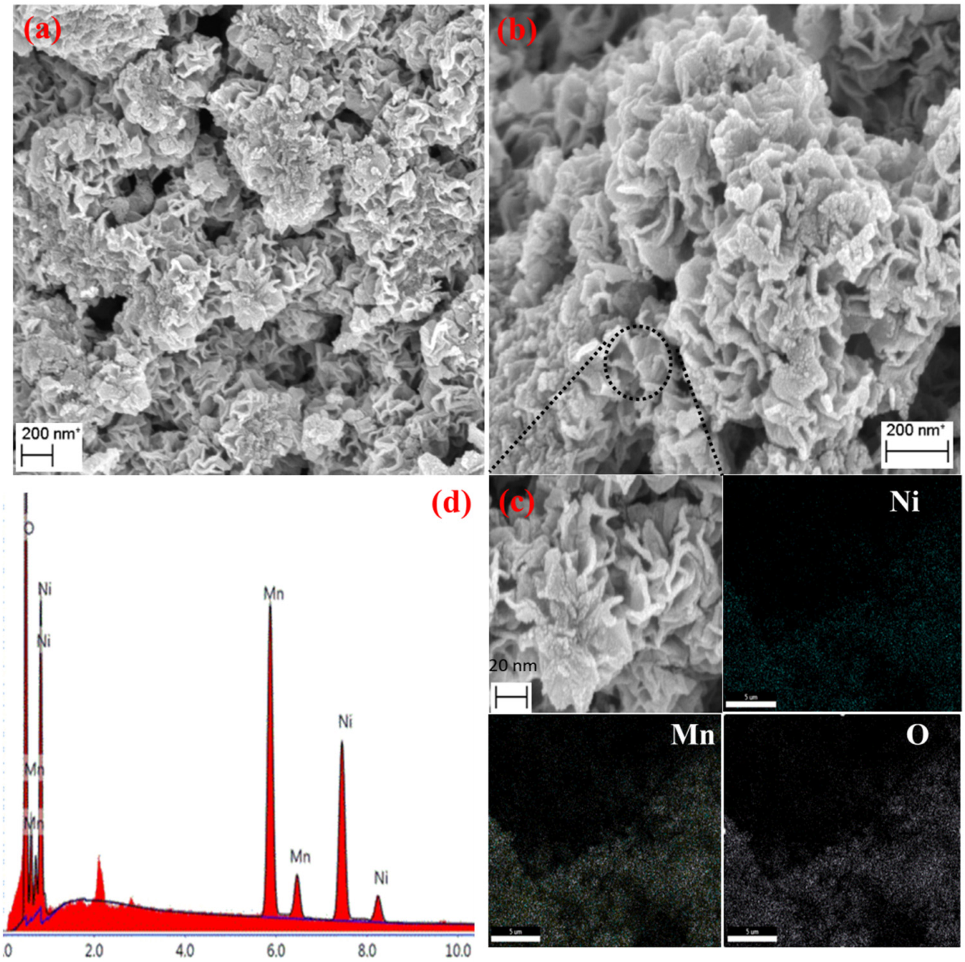

Fig. 2 (a)–(c) FESEM images, (d) EDX spectrum and elemental mapping of the NiO/Mn_3O_4 heterojunction (NM-I).

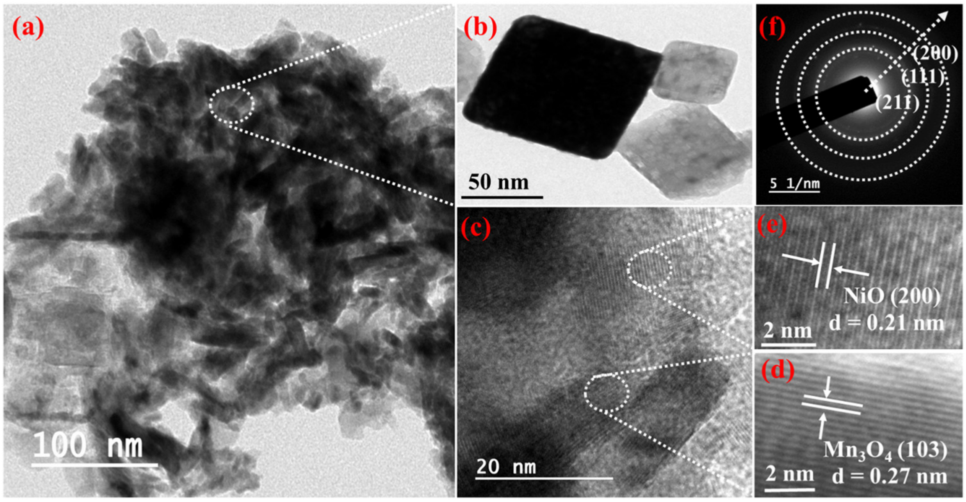

Fig. 3 (a)–(e) HRTEM micrographs and (f) SAED pattern of the NiO/Mn_3O_4 heterojunction (NM-I).

0.1859 cm^3 g^{-1}, respectively. Because it has a relatively particular outer region and a precise pore structure, the NiO/Mn_3O_4 heterojunction is favourable for surface interactions.

3.1.7 **Elemental analysis.** The XPS technique was used to analyse the chemical composition and electronic state of the prepared NiO/Mn_3O_4 heterojunction (Fig. 4). The survey scan of

Open Access Article. Published on 10 September 2024. Downloaded on 2/24/2026 11:31:03 PM.
This article is licensed under a Creative Commons Attribution 3.0 Unported Licence.

the heterojunction (Fig. 4(a)) indicated the presence of Ni, Mn, O, and C elements. Ni $2p_{3/2}$ and Ni $2p_{1/2}$ peaks are supported by the obtained Ni 2p spectra. The typical peaks of Ni^{2+} $2p_{3/2}$ and its satellite peaks were discovered at 854.5 and 861.2 eV, respectively, while the peak of Ni^{2+} $2p_{1/2}$ was discovered at 872.1 and 878.8 eV (Fig. 4(b)), demonstrating the formation of NiO structures.[38] The Mn 2p binding energies are 641.7 eV and 653.1 eV, respectively, (Fig. 4(c)) and are related to the Mn $2p_{3/2}$ and Mn $2p_{1/2}$ peaks, respectively. The presence of Mn $2p_{3/2}$ and Mn $2p_{1/2}$ binding energies shows that the element Mn is in a +2 oxidation state (Mn^{2+}). The deconvoluted O 1s spectra (Fig. 4(d)) indicated two binding energies at 529.2 eV and 530.8 eV, which are related to Ni–O and Mn–OH, respectively.[39] The oxide form of oxygen bound with the metals is adequately supported by the position of the primary binding energy at 529.2 eV. The deconvoluted spectra of C 1s (Fig. 4(e)) exhibited two peaks at 284.3 and 286.3 eV, which are attributed to the C–OH/C–O–Ni and C–C/CQC, respectively. The survey spectra of the pure NiO and Mn_3O_4 NPs are displayed in Fig. S6 (ESI†).

3.2 Estimation of catalytic activity of NiO/Mn_3O_4 heterojunction

Photocatalytic degradation of thiamethoxam over NiO/Mn_3O_4 heterojunction. The photocatalytic degradation of the

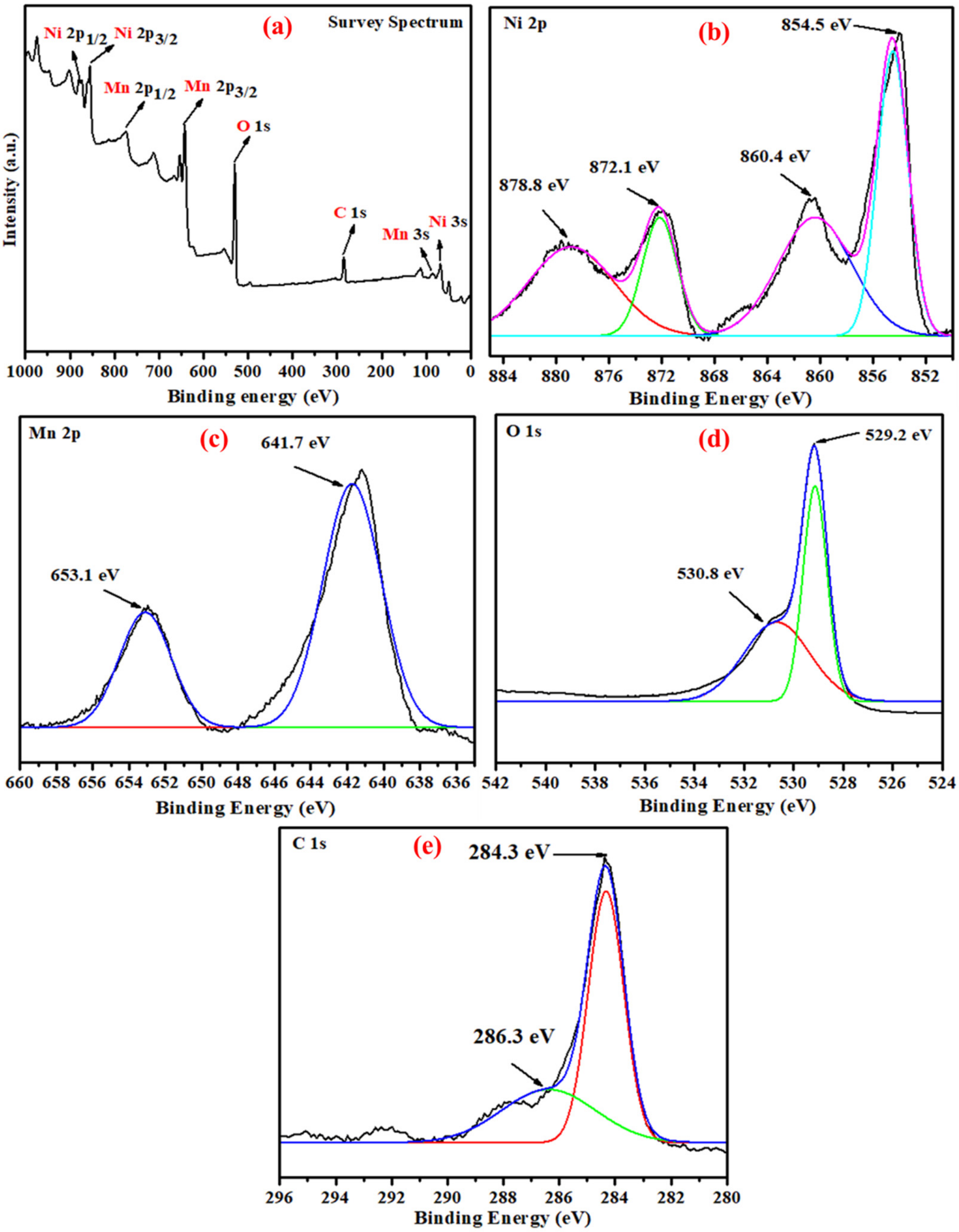

Fig. 4 High resolution XPS spectra of the NiO/Mn_3O_4 heterojunction (NM-I).

© 2024 The Author(s). Published by the Royal Society of Chemistry

Open Access Article. Published on 10 September 2024. Downloaded on 2/24/2026 11:31:03 PM. This article is licensed under a Creative Commons Attribution 3.0 Unported Licence.

thiamethoxam (TMX) pesticide in an aqueous solution was performed under UV radiation to determine the performance of the prepared photocatalysts. The UV-vis spectrum of TMX during photocatalytic degradation is shown in Fig. 5. A maximum of 93% decomposition of TMX was attained by NiO/Mn_3O_4 heterojunction after 90 min of irradiation (Fig. 5(a)).

A photocatalyst-free TMX solution was employed as the standard to determine the direct photolysis of TMX under light irradiation. It is evident from Fig. 5(b) that only 3.2% of TMX was degraded after 90 min of illumination, indicating that the self-degradation of TMX is negligible in the absence of NiO/Mn_3O_4 heterojunction photocatalyst. After adding NiO/Mn_3O_4 heterojunction photocatalyst, the TMX underwent decomposition with time at a steady rate. The diminution in TMX concentration is due to the redox reactions occurring on the surface of the heterojunction through excellent electron–hole splitting.[9]

The degradation of TMX pesticide in sunlight was reported to be 37.4% and 40.1% for NiO and Mn_3O_4 semiconductors after 90 min, respectively. An exceptional improvement in TMX decomposition was observed in this photocatalytic experiment for NiO/Mn_3O_4 heterojunctions (93% for NM-I, 67.8% for NM-II, and 64.3% for NM-III) in just 90 min of exposure. The degradation efficiency which is twice that of solo NiO or Mn_3O_4, was attained with NM-I. The suppressed charge carrier recombination, an appropriate band arrangement between both semiconductors, namely NiO and Mn_3O_4, as well as a broad-spectrum response, contributed to the remarkable performance of NM-I.

Fig. 5(c) shows the plots of $\ln(C_0/C_t)$ *vs.* time of exposure for each of the photocatalysts. The observed linear graphs demonstrate that pseudo-first-order reaction kinetics govern the breakdown of TMX. The rate constant (k) for the photocatalytic experiments was calculated from the slopes of these graphs. The heterojunction NM-I had the highest rate constant ($0.0212\ \text{min}^{-1}$) for TMX (Fig. 5(c)), while the NiO, Mn_3O_4, NM-II, and NM-III samples had rate constants of 0.0059, 0.0063, 0.0141, and 0.0128 min^{-1}, respectively. The rate constant of the NM-I heterojunction demonstrated that the photocatalytic activity of this heterojunction is higher than that of pure NiO and Mn_3O_4 semiconductors.

3.3 Impact of various parameters on photocatalytic performance

3.3.1 Catalyst loading effect. The decomposition efficiency of photocatalysis is greatly affected by the photocatalyst dosage.

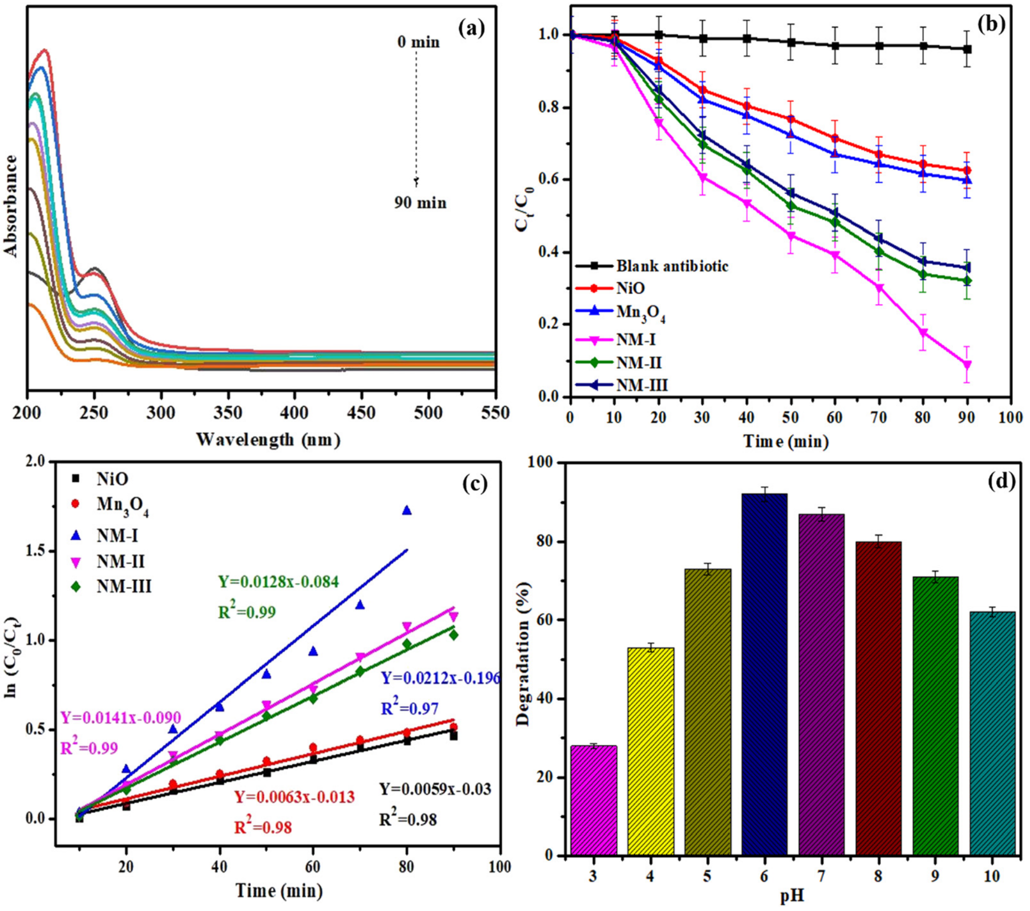

Fig. 5 (a, b) UV-vis absorbance plots (c) plot of $\ln(C_0/C_t)$ against time, and (d) pH effect on the photocatalytic degradation of thiamethoxam with the NiO/Mn_3O_4 heterojunction.

Open Access Article. Published on 10 September 2024. Downloaded on 2/24/2026 11:31:03 PM. This article is licensed under a Creative Commons Attribution 3.0 Unported Licence.

Varying amounts (10, 20, 30, and 40 mg) of the photocatalyst were put separately in the aqueous solutions of pesticide (30 mg L^{-1}). The outcomes of the current study (Fig. S8, ESI†) showed that the efficiency of degradation for 10, 20, 30, and 40 mg of catalyst was 39.2%, 72.4%, 93.1%, and 93.3%, respectively. This is because the increased catalyst loading created more active sites for redox reactions and irradiation created more charge carriers involved in oxidation–reduction reactions.[40] It is noteworthy that the efficiency of degradation for TMX was nearly identical at catalyst dosages of 30 and 40 mg. Increased photocatalyst loading results in saturation, which increases the solution dispersion and has implications, including light accumulation and screening. Consequently, the ability of the photocatalyst to absorb light was subsequently reduced. Therefore, to carry out further investigations on the decomposition of the TMX pesticide, 30 mg of the photocatalyst dose was chosen.

3.3.2 Effect of pH. The pH of a particular solution is crucial for photocatalytic reactions, as the interactions among the pollutants and the photocatalyst surface extremely depend on the pH of the sample.[41] The photocatalyst, NiO/Mn_3O_4, heterojunction is chemically stable and demonstrates a point of zero charge nearly at pH = 6.3 (Fig. S9, ESI†), suggesting that it may become positively charged below this pH value and negatively charged above this pH. Contrarily, polarisation is required for the pesticides to be charged negatively, and some studies have found that the half-life of TMX is shortened under highly alkaline conditions.[10,42] The experiments were carried out at a concentration of 30 mg L^{-1} for TMX, and the pH was carefully adjusted by the inclusion of (0.1 M) HCl or NaOH. The role of pH on the photocatalytic decomposition efficacy of TMX was explored in the pH range 3–10 in the presence of NiO/Mn_3O_4 heterojunction. The change in the degradation efficiency of TMX with respect to pH is depicted in Fig. 5(d). This is understandable that photocatalytic decomposition efficiency rises from a highly to weakly acidic environment. The ideal pH was discovered at 5.8, which is the expected pH of the TMX suspension in NiO/Mn_3O_4 heterojunction. Meanwhile, the pH_{pzc} of NiO/Mn_3O_4 heterojunction is nearly 6.3, and the NiO/Mn_3O_4 surface acquires a positive charge in an acidic environment ($pH < 6.3$), while it acquires a negative charge in an alkaline environment ($pH > 7$).

At a natural pH value (pH = 5.8), the NiO/Mn_3O_4 surface has a weak positive charge, while TMX is mainly neutral, which helps in the adsorption of the substrate, thus promoting photocatalytic decomposition. The low deterioration of TMX in a highly alkaline medium might be due to the repulsions between the hydroxide ions of TMX and the negatively charged NiO/Mn_3O_4 heterojunction over the point of zero charge of the NiO/Mn_3O_4 heterojunction ($ZPC_{NiO/Mn_3O_4} = 6.3$), which ultimately surpasses the beneficial effect resulting from the higher hydroxide ion concentration.[42]

The photocatalytic activity of NM-I was ascertained and compared with various recently published photocatalysts (Table 1), which signifies the impressive capability of NiO/Mn_3O_4 heterojunction for water treatment.

3.3.3 Mechanism of the photocatalytic degradation. The active radicals generated during photocatalysis are crucial in the process of degrading TMX; hence, radical trapping experiments were carried out.[27] Fig. S10 (ESI†) displays the inhibitory effect of different scavengers on NiO/Mn_3O_4 heterojunction. Benzoquinone (BQ), isopropyl alcohol (IPA), triethyl amine (TEA) and $K_2Cr_2O_7$ were engaged as scavengers for $^{\bullet}O_2^{-}$ radicals, $^{\bullet}OH$ radicals, holes (h^+) and electrons (e^-), respectively. These studies were conducted under the same conditions as the photocatalytic examinations. As displayed in Fig. S6 (ESI†), the addition of BQ and $K_2Cr_2O_7$ had only a negligible effect on TMX decomposition, while IPA and TEA largely inhibited TMX decomposition. Hence, it is evident that $^{\bullet}OH$ radicals and holes (h^+) play a primary function in the photocatalytic degradation of TMX.

Identification of the degradation by-products of TMX

During the degradation of Thiamethoxam, various intermediates were identified using the LC–MS method, and major peaks were observed in the spectra (Fig. S11, ESI†). Several intermediates were recognized, *viz. m*/*z* 274, *m*/*z* 211, *m*/*z* 258, and *m*/*z* 102. A literature survey confirmed that these intermediates existed in TMX decomposition. These findings reveal three possible degradation pathways: nitrate reduction, C–N cleavage

Table 1 Comparison of different photocatalysts for the degradation of TMX, CV and RhB

Material	Contaminant	% Deterioration	Light source	Time (min)	Contaminant concentration (g L^{-1})	Amount of dosage (g L^{-1})	Ref.
$qSnO_2/GO$	RhB	95	Sunlight	120	0.019	1.6	43
$LaFeO_3/Ag_2CO_3$	RhB	99.5	Sunlight	45	0.00048	1.0	44
SnO_2–ZnS	RhB	95	Sunlight	90	0.01	1.0	45
ZnO	TMX	77	UV	120	0.1	2.0	46
$g\text{-}C_3N_4\text{-}TiO_2$@LMPET	TMX	97	Sunlight	180	0.0058	4.3	47
TiO_2	TMX	99	UV	90	0.01	0.1	48
TiO_2 onto glass slides	TMX	90.1	UV	120	0.1	0.24	49
BiSe-CM	CV	96.3	Sunlight	150	0.03	10.0	50
GO/NiS	CV	93	Sunlight	70	0.008	0.4	51
CuO/Fe_2O_3	RhB	96	Visible	40		0.2	27
NiO/Mn_3O_4	TMX	93.0	Sunlight	90	0.02	0.3	The present study
	RhB	93.6		80			
	CV	93.2		80			

Open Access Article. Published on 10 September 2024. Downloaded on 2/24/2026 11:31:03 PM.
This article is licensed under a Creative Commons Attribution 3.0 Unported Licence.

between the 2-chlorothiazole ring and oxadiazine, and dechlorination. The elimination of $-NO_2$ from TMX led to the intermediate $C_8H_{11}ClN_4OS$, *m*/*z* 246.[52] Another intermediate, $C_3H_7N_3O$, *m*/*z* 101, was observed in the degradation pathway, as reported in the literature.[53] After the elimination of $-NO_2$ from TMX, further dechlorination resulted in the formation of $C_8H_{12}N_4OS$ and *m*/*z* 212 $[M + H]^+$. The C–N bond is an important linkage in most neonicotinoid pesticide molecules. Two similar intermediates were produced when the 2-chlorothiazole ring and oxadiazine's C–N link broke, *i.e.* *N*-(3-methyl-1,3,5-oxadiazinan-4-ylidene)nitramide and 3-methyl-1,3,5-oxadiazinan-4-imine. The oxadiazine formed after the breakage of the C–N bond produced 3-methyl-1,3,5-oxadiazinan-4-imine *via* nitrate reduction. The *N*-nitro tip is reduced to the *N*-nitroso- and *N*-aminoguanidines (*m*/*z* 131) and produces the corresponding =NH (guanidine) (*m*/*z* 115) $[M + H]^+$ and =O (urea), a characteristic decomposition path of neonicotinoid pesticides. A possible pathway for the degradation of TMX and the formation of intermediates is shown in Fig. 6.

3.4 Breakdown of organic dyes

By observing the absorbance at 585 and 554 nm, respectively, the photocatalytic efficacy of the NiO/Mn_3O_4 heterojunction for the decomposition of CV and RhB dyes in sunlight was examined, respectively (Fig. 7(a) and (b)). The photocatalytic efficiency of NiO/Mn_3O_4 heterojunction was examined with variation in pH of the experimental solution, dosage of catalyst, and time to optimize degradation effects. Dye degradation over NiO/Mn_3O_4 heterojunction was studied in the pH range of 3–10 (Fig. S12, ESI†). It was observed that both the dyes (CV and RhB) deteriorated faster in a neutral medium compared to the basic and acidic media. This could be the result of leaching of the NiO/Mn_3O_4 heterojunction in solution, which forms chemical sludge under basic conditions, and Fenton's reagent in acidic mixtures.

The impact of the catalyst dose on the photo-decomposition efficiency of CV and RhB dyes was also investigated. The photo-decomposition efficacy was enhanced from 40.1% to 93.9% (CV dye) and 39.7% to 93.6% (RhB dye) as the NM-I dose was increased from 10 to 40 mg. However, increasing the NM-I dose from 30 to 40 mg resulted in a negligible improvement in photo-degradation efficiency for CV and RhB. Beyond a particular level, increasing the catalyst dose decreases the percentage of deterioration because the catalyst particles clump together in solution, which block light penetration and photon absorption. The best dose of NM-I for the degradation of CV and RhB dyes is 30 mg based on the optimization results.

Consequently, the NiO/Mn_3O_4 heterojunction photocatalyst demonstrated greater efficacy in degrading the neutral dye solution. It has been observed that 62.7%, 66.1%, 93.6%, 85.9% and 83.8% of CV dye (Fig. 8(a)), and 66.2%, 73.7%, 93.2%, 84.7% and 82.5% of RhB dye (Fig. 8(b)) were decomposed with NiO, Mn_3O_4, NM-I, NM-II and NM-III of NiO/Mn_3O_4 heterojunction, respectively, after 80 min of revelation to sunlight. Thus, the heterojunction (NM-I) exhibited the highest photocatalytic efficiency under sunlight exposure.

Further, a negligible amount of CV and RhB dyes degraded under similar experimental conditions without the inclusion of a photocatalyst. However, a significant quantity of dyes vanished when a photocatalyst was added to the dye solutions,

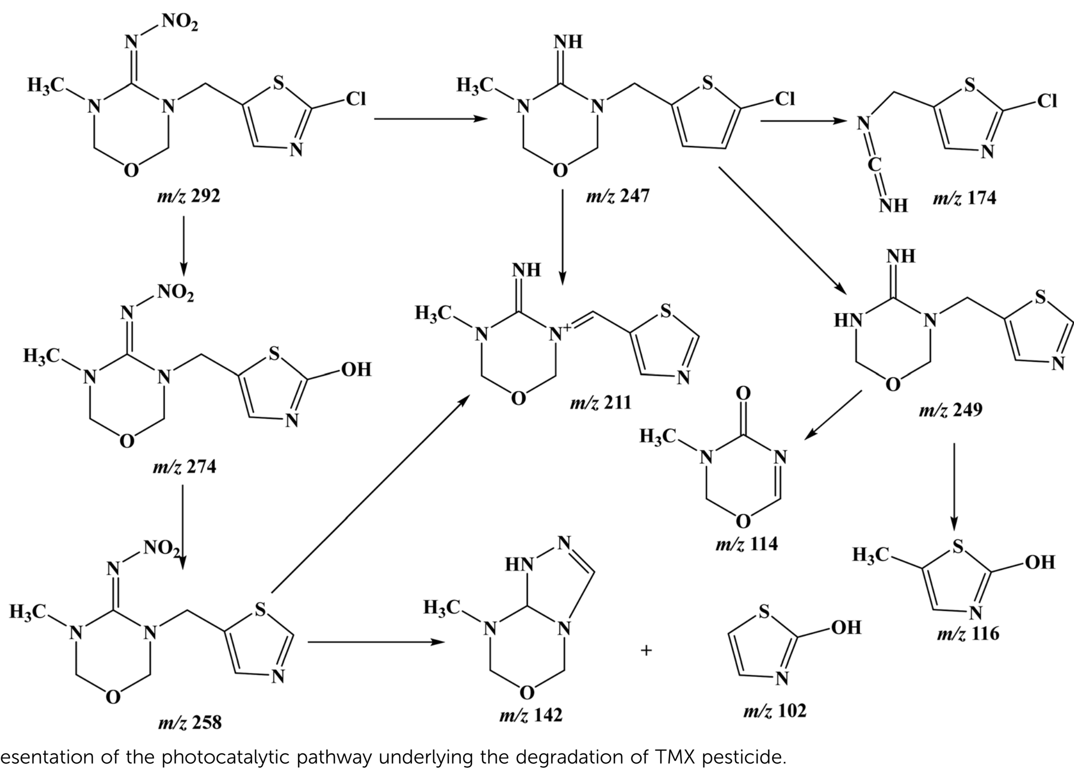

Fig. 6 Representation of the photocatalytic pathway underlying the degradation of TMX pesticide.

© 2024 The Author(s). Published by the Royal Society of Chemistry

Open Access Article. Published on 10 September 2024. Downloaded on 2/24/2026 11:31:03 PM.
This article is licensed under a Creative Commons Attribution 3.0 Unported Licence.

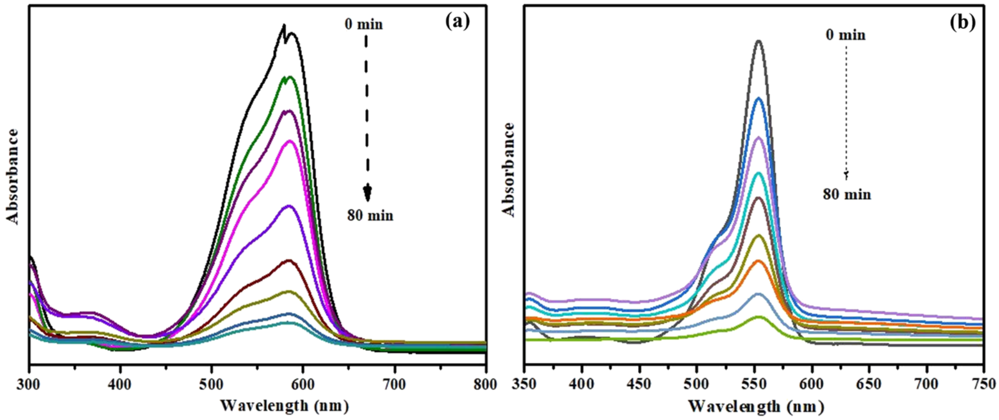

Fig. 7 UV-vis spectrum of degradation of (a) CV and (b) RhB dye solution with the NiO/Mn_3O_4 heterojunction.

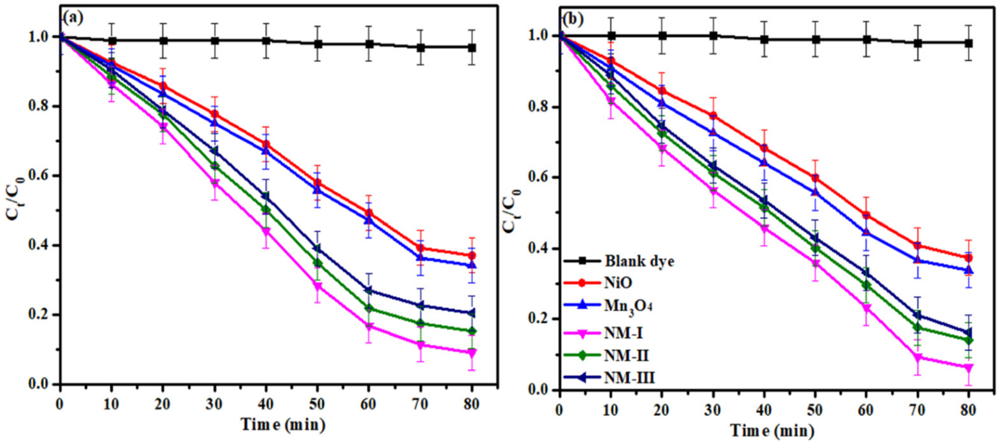

Fig. 8 Concentration changes as a function of irradiation time for (a) CV and (b) RhB dyes.

indicating that the decomposition of dyes is mainly facilitated by photocatalysis.

The degradation kinetics were further explored using the first-order kinetic model to tailor the decomposition data (Fig. 9). It is evident that the experimental records abide by the first-order kinetic model and the R^2 value for both CV and RhB dyes was found to be ≤ 0.95 for all the photocatalyst samples.

For the degradation of CV dye over NiO, Mn_3O_4, NM-I, NM-II and NM-III heterojunction catalysts, the rate constants (*k*) were

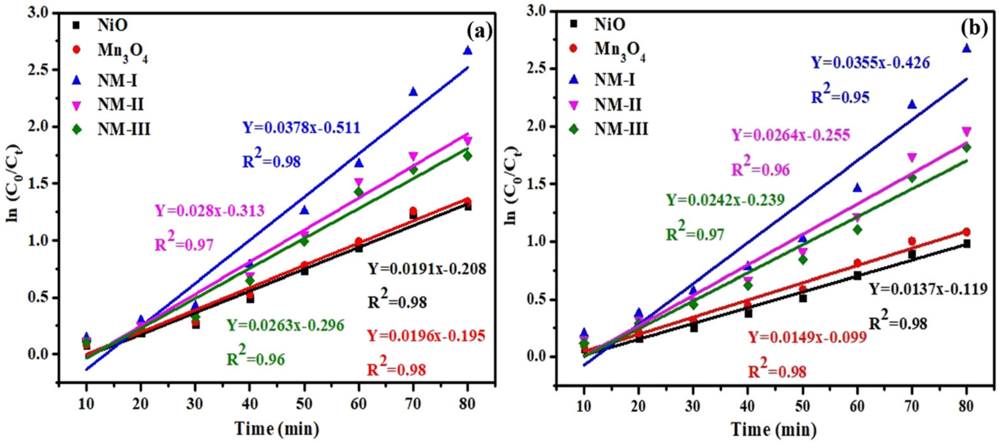

Fig. 9 Degradation rate constants of (a) CV and (b) RhB dyes.

Open Access Article. Published on 10 September 2024. Downloaded on 2/24/2026 11:31:03 PM.
This article is licensed under a Creative Commons Attribution 3.0 Unported Licence.

estimated to be 0.0191, 0.0196, 0.0378, 0.0281, and 0.0263 min^{-1}, respectively. Similarly, for the degradation of RhB dye, over NiO, Mn_3O_4, NM-I, NM-II and NM-III heterojunction catalysts, the rate constants (k) were calculated to be 0.0137, 0.0149, 0.0355, 0.0264, and 0.0242 min^{-1}, respectively. Obviously, the NM-I heterojunction possessed excellent photocatalytic activity under sunlight radiation compared to the other samples.

Reactive species trapping research was carried out using multiple radical quenchers to further comprehend the mechanism of photocatalysis. Chemical substances known as quenchers trap specific species in a photocatalytic study and prevent them from taking part in breakdown reactions. Similar to the TMX, BQ, IPA, TEA and $K_2Cr_2O_7$ were employed as $^{\bullet}O_2^{-}$, $^{\bullet}OH$, h^+ and e^- scavengers, respectively. The scavenging studies were conducted under the same conditions as those of the photocatalytic examinations. Without any quenchers, the control experiment was performed under comparable circumstances. The presence of quenchers significantly decreased the photocatalytic degradation efficiency.

As displayed in Fig. S13 (ESI†), the addition of BQ and $K_2Cr_2O_7$ slightly reduced the degradation process of both CV and RhB dyes, while the degradation efficiency was reduced drastically by up to 20% with the introduction of IPA and TEA scavengers. This indicates that the reactive species $^{\bullet}OH$ and holes h^+ play a significant role in the degradation mechanism. Consequently, it may be assumed that $^{\bullet}OH$ and holes h^+ formed in the photocatalytic system are accountable for the better photooxidation execution towards the degradation procedure.

In the NiO/Mn_3O_4 heterojunction, the interface between NiO and Mn_3O_4 generated improved band structures. The method described earlier[54,55] was used to determine the edge potentials of the conduction band (CB) and valence band (VB). The values of E_g, E_{CB} and E_{VB} calculated by the above method are shown in Table S1 (ESI†).

NiO and Mn_3O_4 were stimulated to create e^- and h^+ at the CB and VB, respectively, upon exposure to sunlight (Fig. 10). The band positions of Mn_3O_4 were below the CB of NiO. The h^+ were transferred from Mn_3O_4 to NiO, and photo excited e^- migrated from NiO to Mn_3O_4. The O_2 in the contaminated solution combined with the e^- to form the superoxide radical ($^{\bullet}O_2^{-}$), and the h^+ produced hydroxyl radical ($^{\bullet}OH$) on reaction with water.

The photocatalytic activity of the NiO/Mn_3O_4 heterojunction was further investigated by assessing the chemical oxygen demand (COD) of dye solutions before and after light introduction in the company of a photocatalyst. CV dye solution's COD decreased from 293 to 82 mg L^{-1} and RhB dye solution's COD decreased from 215 to 84 mg L^{-1}, respectively. Following radiation exposure, the heterojunction's mineralization yield was calculated to be 69% for the CV and 63% for the RhB dye.

3.5 Durability and usefulness of the NM-I heterojunction as a photocatalyst

To ascertain the stability and applicability of the NiO/Mn_3O_4 heterojunction in the photocatalysis of TMX, CV, and RhB under solar light, recycling studies were conducted. The NiO/Mn_3O_4 heterojunction maintained approximately 87% of its photocatalytic activity even after four consecutive runs (Fig. S14, ESI†). The slight drop in the efficiency of degradation in the fourth cycle may be caused by impurities and surface-

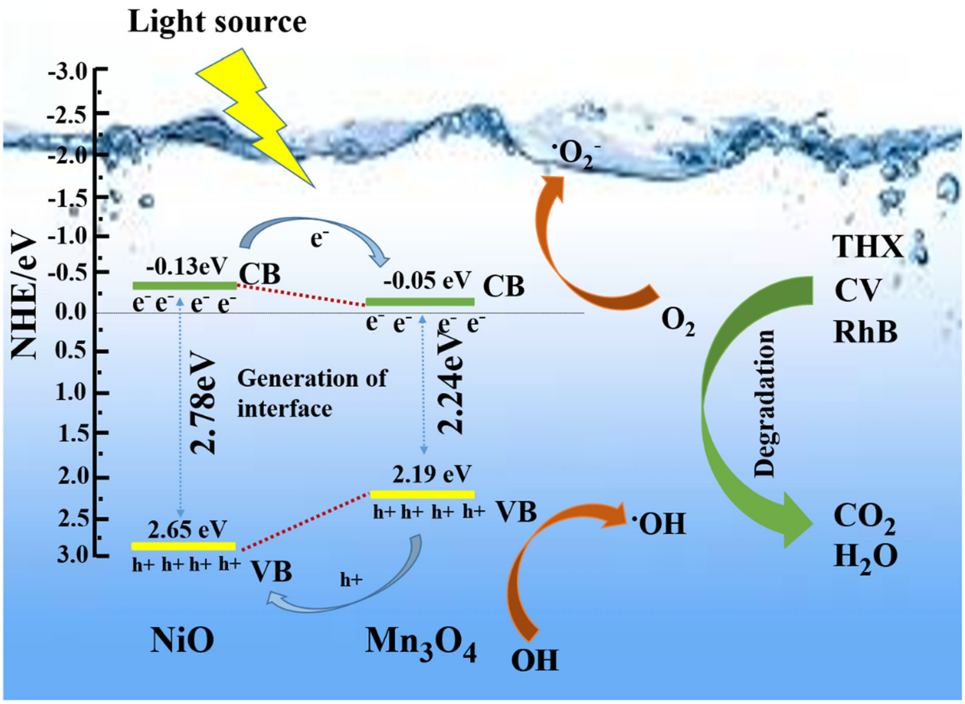

Fig. 10 A tenable approach to eliminating organic contaminants over the NiO/Mn_3O_4 heterojunction in direct sunlight.

Open Access Article. Published on 10 September 2024. Downloaded on 2/24/2026 11:31:03 PM.
This article is licensed under a Creative Commons Attribution 3.0 Unported Licence.

generated intermediates that block the active sites. Centrifugation was used to extract the solid form of the NiO/Mn_3O_4 catalyst; and then, sample washing and calcination were used to eliminate any remaining impurities. Further, it was observed from the XRD studies that the crystallinity of the NM-I heterojunction photocatalyst was maintained (Fig. S15, ESI†). The results reported here suggest that a fabricated heterojunction with high activity is both recyclable and almost durable.

4. Conclusion

The fabrication of NiO/Mn_3O_4 heterojunction photocatalyst using the hydrothermal method has been reported. The fabricated NiO/Mn_3O_4 nanocomposite possessed a nano-size and crystalline nature. The fabricated heterojunction was explored as a photocatalyst for the degradation of CV and RhB dyes, and TMX pesticide. The photodecomposition efficiency of the heterojunction was affected by variations in catalyst amount, irradiation time, and pH. The scavenging studies revealed that the holes (h^+) and $^•OH$ radicals play a major role in the degradation of pollutants. The results divulged that the NiO/Mn_3O_4 heterojunction is an efficient photocatalyst for the decomposition of CV and RhB dyes as well as TMX pesticide under sunlight radiation, without any detrimental effect on the environment. The kinetics of the photocatalysis reaction revealed 93%, 81.2% and 91.2% decomposition of the TMX, CV, and RhB pollutants, respectively, in 90, 115 and 90 min under the optimum conditions. The fabricated materials have proven to be potential photocatalysts for promoting the elimination of organic pollutants based on photocatalytic investigations. This work presents an environmentally safe and non-toxic way of synthesizing heterojunctions by employing an eco-friendly preparation process. It also showcases the progress made in photocatalysis, which will be helpful for future research in industrial applications.

Author contributions

Conceptualization: Sandeep Kaushal, Mandvi and Prit Pal Singh; methodology: Sandeep Kaushal, Sandeep Kumar, and Prit Pal Singh; validation: Sandeep Kaushal and Prit Pal Singh; formal analysis: Sandeep Kaushal, Suhas Ballal, Mamta Chahar, Jaya Bansal, Ranvijay Kumar; writing – original draft: Sandeep Kaushal; writing – review and editing: Sandeep Kaushal and Prit Pal Singh; supervision: Sandeep Kaushal and Prit Pal Singh. All the authors have read and agreed to the published version of the manuscript.

Data availability

The data that support the findings of this study are available from the Royal Society of Chemistry, but restrictions apply to the availability of these data, which were used under license for the current study, and therefore are not publicly available. Data are however available from the authors upon reasonable request and with permission from the Royal Society of Chemistry.

Conflicts of interest

The authors declare no competing interests.

References

1 N. Nemanja Banic, V. Abramovic, J. Krstic, D. Sojic, D. Loncarevic, Z. Zheleva and V. Guzsvany, Photodegradation of thiacloprid using Fe/TiO_2 as a heterogeneous photo-Fenton catalyst, *Appl. Catal., B*, 2011, **107**, 363–371.

2 M. Syafrudin, R. Kristanti, A. Yuniarto, T. Hadibarata, J. Rhee, W. A. Alonazi, T. S. Algarni, A. H. Almarri and A. Mohaimeed, Pesticides in drinking water—A review, *Int. J. Environ. Res. Public Health*, 2021, **18**(2), 468.

3 A. Sharma, V. Kumar, B. Shahzad, M. Tanveer, G. Sidhu and A. Thukral, Worldwide pesticide usage and its impacts on ecosystem, *SN Appl. Sci.*, 2019, **1**, 1446.

4 W. Aktar, D. Sengupta and A. Chowdhary, Impact of pesticides use in agriculture: their benefits and hazards, *Interdiscip. Toxicol.*, 2009, **2**(1), 1–12.

5 R. H. Coup and J. D. Blomquist, Water-soluble pesticides in finished water of community water supplies, *J. – Am. Water Works Assoc.*, 2004, **96**, 56–68.

6 M. Tudi, H. D. Ruan, L. Wang, J. Lyu, R. Sadler, D. Conell, C. Chu and D. Phung, Agriculture development, pesticide application and its impact on the environment, *Int. J. Environ. Res. Public Health*, 2021, **18**(3), 1112.

7 N. D. Banic, D. V. Sojic, J. B. Krstic and B. F. Abramovic, Photodegradation of neonicotinoid active ingredients and their commercial formulations in water by different advanced oxidation processes, *Water, Air, Soil Pollut.*, 2014, **225**, 1954.

8 N. A. Mir, A. Khan, M. Muneer and S. Vijyalakhsmi, Photocatalytic degradation of a widely used insecticide Thiamethoxam in aqueous suspension of TiO_2: Adsorption, kinetics, product analysis and toxicity assessment, *Sci. Total Environ.*, 2013, **458–460**, 388–398.

9 P. B. Patil, S. Jadhav and A. B. Pandit, Effect of intensifying additives on the degradation of thiamethoxam using ultrasound cavitation, *Ultrason. Sonochem.*, 2021, **70**, 105310.

10 H. Yang, H. Liu, Z. Hu, J. Liang, H. Pang and B. Yi, Consideration on degradation kinetics and mechanism of thiamethoxam by reactive oxidative species (ROSs) during photocatalytic process, *J. Chem. Eng.*, 2014, **245**, 24–33.

11 E. Serano, M. Munoz, Z. Pedro and J. Casas, Fast oxidation of the neonicotinoid pesticides listed in the EU Decision 2018/840 from aqueous solutions, *Sep. Purif. Technol.*, 2020, **235**, 116168.

12 D. Sojic, V. Despotovic, D. Orcic, E. Szabo, E. Arany, S. Armakovic and B. Abramovic, Degradation of thiamethoxam and metoprolol by UV, O_3 and UV/O_3 hybrid processes:

© 2024 The Author(s). Published by the Royal Society of Chemistry

Open Access Article. Published on 10 September 2024. Downloaded on 2/24/2026 11:31:03 PM.
This article is licensed under a Creative Commons Attribution 3.0 Unported Licence.

Kinetics, degradation intermediates and toxicity, *J. Hydrol.*, 2012, **472–473**, 314–327.

13 M. Rashid, M. Ikram, A. Haider, S. Naz, J. Haider, A. Hamid, A. Shahzadi and M. Aqeel, Photocatalytic, dye degradation, and bactericidal behavior of Cu-doped ZnO nanorods and their molecular docking analysis, *Dalton Trans.*, 2020, **49**, 8314–8330.

14 V. Jayarama, C. Ayappan, B. Palanivel and A. Mani, Bridging and synergistic effect of the pyrochlore like $Bi_2Zr_2O_7$ structure with robust CdCuS solid solution for durable photocatalytic removal of the organic pollutants, *RSC Adv.*, 2020, **10**, 8880–8894.

15 H. Zhu, R. Jiang, L. Xiao, Y. Chang, Y. Guan, X. Li and G. Zeng, Photocatalytic decolorization and degradation of Congo Red on innovative crosslinked chitosan/nano-CdS composite catalyst under visible light irradiation, *J. Hazard. Mater.*, 2009, **169**, 933–940.

16 S. Ghosh, N. Kouame, L. Ramos, S. Remita, A. Dazzi, A. Besseau, P. Beaunier, F. Goubard, P. Aubert and H. Remita, Conducting polymer nanostructures for photocatalysis under visible light, *Nat. Mater.*, 2015, **14**, 505–511.

17 A. Daas and O. Hamdauli, Extraction of anionic dye from aqueous solutions by emulsion liquid membrane, *J. Hazard. Mater.*, 2010, **178**, 973–981.

18 Z. Ying, L. Guang, S. Mei, L. Miao, Z. Yu and Z. Cheng, Bacterial Community and Function of Biological Activated Carbon Filter in Drinking Water Treatment, *Biomed. Environ. Sci.*, 2011, **24**, 122–131.

19 P. Zhang, J. Xu, X. Wang, B. He, S. Gao and Y. Lin, The Third Generation of Artificial Dye-Decolorizing Peroxidase Rationally Designed in Myoglobin, *ACS Catal.*, 2019, **9**, 7888–7893.

20 X. Zhang, Y. Liu, Q. Nan, J. Hou, B. Zuo, C. Hu, L. Hu, J. Tang and X. Liu, In-situ dispersing ultrafine Fe_2O_3 nanoparticles in mesoporous silicas for efficient peroxymonosulfate-activated degradation of tetracycline over a broad pH range, *J. Environ. Chem. Eng.*, 2022, **10**, 106904.

21 S. Sasi, P. Fasna, T. Sharmilla, C. Chandra, J. Antony, V. Raman, A. Nair and H. Ramanathan, Green synthesis of ZnO nanoparticles with enhanced photocatalytic and antibacterial activity, *J. Alloys Compd.*, 2022, **924**, 166431.

22 B. Sahin, R. Aydin and H. Cetin, Tuning the morphological, structural, optical and dielectric properties of hausmannite (Mn_3O_4) films by doping heavy metal lead, *Superlattices Microstruct.*, 2020, **143**, 106546.

23 C. J. Pandian, R. Palanivel and S. Dhananasekram, Green synthesis of nickel nanoparticles using Ocimum sanctum and their application in dye and pollutant adsorption, *Chin. J. Chem. Eng.*, 2015, **23**, 1307–1315.

24 C. Kumar, V. S. Betageri, G. Nagaraju, G. H. Pujar, B. P. Suma and M. S. Latha, Photocatalytic, nitrite sensing and antibacterial studies of facile bio-synthesized nickel oxide nanoparticles, *J. Sci. Adv. Mater. Devices*, 2020, **5**, 48–55.

25 Y. Singh, R. S. Sodhi, P. Singh and S. Kaushal, Biosynthesis of NiO nanoparticles using Spirogyra sp. cell-free extract and their potential biological applications, *Mater. Adv.*, 2022, **3**, 4991.

26 V. Kumari, S. Kaushal and P. Singh, Green synthesis of a CuO/rGO nanocomposite using a Terminalia arjuna bark extract and its catalytic activity for the purification of water, *Mater. Adv.*, 2022, **3**, 2170.

27 S. Kaushal, A. Kumar, H. Bains and P. Singh, Photocatalytic degradation of tetracycline antibiotic and organic dyes using biogenic synthesized CuO/Fe_2O_3 nanocomposite: pathways and mechanism insights, *Environ. Sci. Pollut. Res. Int.*, 2023, **30**, 37092–37104.

28 Y. Singh, S. Kaushal and R. M. Sodhi, Biogenic synthesis of silver nanoparticles using cyanobacterium Leptolyngbya sp. WUC 59 cell-free extract and their effects on bacterial growth and seed germination, *Nanoscale Adv.*, 2020, **2**, 3972.

29 K. Bano, S. Kaushal, A. Kumar and P. Singh, Sunlight-driven photocatalytic degradation of 4-nitrophenol and adsorptive removal of Mn(II) ions from industrial wastewater by biogenic synthesized CuO/SnO_2 heterojunction, *Mater. Today Chem.*, 2022, **26**, 101193.

30 K. Bano, S. Kaushal, B. Lal, S. K. Joshi, R. Kumar and P. P. Singh, Fabrication of CuO/ZnO heterojunction photocatalyst for efficient photocatalytic degradation of tetracycline and ciprofloxacin under direct sun light, *Environ. Nanotechnol., Monit. Manage.*, 2023, **20**, 100863.

31 Parul, K. Kaur, R. Badru, P. P. Singh and S. Kaushal, Photodegradation of organic pollutants using heterojunctions: A review, *J. Environ. Chem. Eng.*, 2020, **8**, 103666.

32 K. Bano, P. P. Singh, S. Kumar, S. M. Saeed, S. Aggarwal, R. Kumar and S. Kuahsl, Construction of honey bee hive-like CuO/PbO heterojunction photocatalysts with enhanced antibiotic and dye degradation activity under visible light, *Environ. Sci.: Water Res. Technol.*, 2024, **10**, 1714.

33 A. A. Amer, S. M. Reda, M. A. Mousa and M. M. Mohamed, Mn_3O_4/graphene nanocomposites: outstanding performances as highly efficient photocatalysts and microwave absorbers, *RSC Adv.*, 2017, **7**, 826.

34 S. J. Hong, H. J. Mun, B. J. Kim and Y. S. Kim, Characterization of nickel oxide nanoparticles synthesized under low temperature, *Micromachines*, 2021, **12**(10), 1168.

35 S. Srihasan, K. Thyagarajan, M. Korivi, V. R. Lebaka and S. P. Mallem, Phytogenic generation of NiO nanoparticles using stevia Leaf extract and evaluation of their *in vitro* antioxidant and antimicrobial properties, *Biomolecules*, 2020, **10**, 89.

36 M. Karimi and M. J. Eshragi, One-pot and green synthesis of Mn_3O_4 nanoparticles using an all-in-one system (solvent, reactant and template) based on ethaline deep eutectic solvent, *J. Alloys Compd.*, 2017, **696**, 171–176.

37 J. K. Sharma, P. Srivastava, S. Ameen, M. S. Akhtar, G. Singh and S. Yadava, Azadirachta indica plant-assisted green synthesis of Mn_3O_4 nanoparticles: Excellent thermal catalytic performance and chemical sensing behaviour, *J. Colloid Interface Sci.*, 2016, **472**, 220–228.

38 Y. M. Hunge, A. A. Yadav, S. Khan, K. Takagi, N. Suzuki and C. Terashima, Photocatalytic degradation of bisphenol A using titanium dioxide@nanodiamond composites under UV light illumination, *J. Colloid Interface Sci.*, 2021, **582**, 1058–1066.

© 2024 The Author(s). Published by the Royal Society of Chemistry

Open Access Article. Published on 10 September 2024. Downloaded on 2/24/2026 11:31:03 PM.
This article is licensed under a Creative Commons Attribution 3.0 Unported Licence.

39 B. Li, C. Lai, G. Zeng, L. Qin, H. Yi and S. Liu, facile hydrothermal synthesis of *Z*-scheme $Bi_2Fe_4O_9/Bi_2Wo_6$ heterojunction photocatalyst with enhanced visible light photocatalytic activity, *ACS Appl. Mater. Interfaces*, 2018, **10**, 18824–18836.

40 Q. Zhang, L. Jiang, J. Wang, Y. Zhu, Y. Pu and W. Dai, Photocatalytic degradation of tetracycline antibiotics using three-dimensional network structure perylene diimide supramolecular organic photocatalyst under visible-light irradiation, *Appl. Catal., B*, 2020, **277**, 119122.

41 A. M. Niyaz, A. Khan, M. Muneer and S. Vijayalakhsmi, Photocatalytic degradation of a widely used insecticide Thiamethoxam in aqueous suspension of TiO_2: Adsorption, kinetics, product analysis and toxicity assessment, *Sci. Total Environ.*, 2013, **460**, 458–460.

42 R. Karmakar, S. B. Singh and G. Kulshrestha, Kinetics and mechanism of the hydrolysis of thiamethoxam, *J. Environ. Sci. Health, Part B*, 2009, **44**, 435–441.

43 G. Rani, G. Kumar, S. Steplinpaulselvin, R. Rajaram, T. S. Silambarasan and Y. Chen, Survival assessment of simple food webs for dye wastewater after photocatalytic degradation using SnO_2/GO nanocomposites under sunlight irradiation, *Sci. Total Environ.*, 2020, **721**, 137805.

44 B. M. Pirzada, Pushpendra, R. K. Kunchala and B. Naidu, Synthesis of $LaFeO_3/Ag_2CO_3$ Nanocomposites for Photocatalytic Degradation of Rhodamine B and p-Chlorophenol under Natural Sunlight, *ACS Omega*, 2019, **4**, 2618–2629.

45 L. Hu, F. Chen, P. Hu, L. Zou and X. Hu, Hydrothermal synthesis of SnO_2/ZnS nanocomposite as a photocatalyst for degradation of Rhodamine B under simulated and natural sunlight, *J. Mol. Catal. A: Chem.*, 2016, **411**, 203–213.

46 N. D. Banic, B. F. Abramovic, D. V. Sojic, J. B. Krstic, N. L. Fincur and I. P. Bockovic, Efficiency of neonicotinoids photocatalytic degradation by using annular slurry reactor, *J. Chem. Eng.*, 2016, **286**, 184–190.

47 Y. Chen, W. Lu, H. Shen, Y. Gu, T. Xu, Z. Zhu, G. Wang and W. Chen, Solar-driven efficient degradation of emerging contaminants by $g\text{-}C_3N_4$-shielding polyester fiber/TiO composites, *Appl. Catal., B*, 2019, **258**, 117960.

48 M. K. Arfanis, G. V. Theodorakopoulos, C. Anagnostopoulos, I. Georgaki, E. Karanasios, G. Romanos, E. Markellou and P. Falaras, Photocatalytic Removal of Thiamethoxam and Flonicamid Pesticides Present in Agro-Industrial Water Effluents, *Catalysts*, 2023, **13**, 516.

49 R. Zabar, T. Komel, J. Fabjan, M. B. Kralj and P. Trebse, Photocatalytic degradation with immobilised TiO(2) of three selected neonicotinoid insecticides: imidacloprid, thiamethoxam and clothianidin, *Chemosphere*, 2012, **89**, 293–301.

50 W. Ahmad, A. Khan, S. Ali, S. Khan, S. Uddin, S. Malik, N. Ali, H. Khan and M. Bilal, Photocatalytic degradation of crystal violet dye under sunlight by chitosan-encapsulated ternary metal selenide microspheres, *Environ. Sci. Pollut. Res.*, 2020, **28**, 8074–8087.

51 V. Manikandan, R. Elancheran, P. Revathip and K. Krishnasamy, Efficient photocatalytic degradation of crystal violet by using graphene oxide/nickel sulphide nanocomposites, *Bull. Mater. Sci.*, 2020, **43**, 265.

52 H. Zhan, Q. Wan, Y. Wang, J. Cheng, X. Yu and J. Ge, An endophytic bacterial strain, Enterobacter cloacae TMX-6, enhances the degradation of thiamethoxam in rice plants, *Chemosphere*, 2021, **269**, 128751.

53 J. Meijide, j Gomez, M. Pazos and M. A. Sanroman, Degradation of thiamethoxam by the synergetic effect between anodic oxidation and Fenton reactions, *J. Hazard. Mater.*, 2016, **319**, 43–50.

54 S. Kaushal, P. Kurichh and P. Singh, Novel 3D flower like ZnO/MnV_2O_6 heterojunction as an efficient adsorbent for the removal of imidacloprid and photocatalyst for degradation of organic dyes in waste water, *Polyhedron*, 2021, **201**, 115161.

55 K. Bano, S. K. Mittal, P. Singh and S. Kaushal, Sunlight driven photocatalytic degradation of organic pollutants using a $MnV_2O_6/BiVO_4$ heterojunction: mechanistic perception and degradation pathways, *Nanoscale Adv.*, 2021, **3**, 6446–6458.

© 2024 The Author(s). Published by the Royal Society of Chemistry